Physics Letters B 738 (2014) 401–404

Contents lists available at ScienceDirect

Physics Letters B

www.elsevier.com/locate/physletb

A region of high-spin toroidal isomers

Andrzej Staszczak [a,*], Cheuk-Yin Wong [b]

[a] Institute of Physics, Maria Curie-Skłodowska University, pl. M. Curie-Skłodowskiej 1, 20-031 Lublin, Poland
[b] Physics Division, Oak Ridge National Laboratory, P.O. Box 2008, Oak Ridge, TN 37831, USA

ARTICLE INFO

Article history:
Received 13 May 2014
Received in revised form 13 September 2014
Accepted 6 October 2014
Available online 11 October 2014
Editor: J.-P. Blaizot

Keywords:
Toroidal light nuclei
High-K isomeric states

ABSTRACT

The combined considerations of both the bulk liquid-drop-type behavior and the quantized angular momentum reveal that high-spin toroidal isomeric states may have general occurrences for light nuclei with $28 \leqslant A \leqslant 52$. High-spin $N = Z$ toroidal isomers in this mass region have been located theoretically using cranked self-consistent constraint Skyrme–Hartree–Fock model calculations.

Nuclei as we now know them have sphere-like geometry. Wheeler suggested that under appropriate conditions the nuclear fluid may assume a toroidal shape [1–3]. Toroidal nuclei are however plagued with various instabilities [3], and the search remains elusive [4–6]. It was found previously from the liquid-drop model that a "rotation" about the symmetry axis with an angular momentum $I = I_z$ above a threshold can stabilize the toroidal nucleus and can lead to a high-spin isomer [7].

The toroidal high-spin isomer, whose large angular momentum $I = I_z$ must be generated by the alignment of individual nucleon angular momenta along the symmetry axis [8], provides an elegant example in quantum mechanics as how an axially-symmetric system can acquire a quantized angular momentum. Furthermore, the nuclear fluid in the toroidal isomeric state may be so severely distorted by the change from sphere-like geometry to the toroidal shape that it may acquire bulk properties of its own, to make it a distinct type of quantum fluid. Finally, the toroidal high-spin isomer may be a source of energy, as its decay to the ground state can release a large amount of excitation energy. The possibility of toroidal high-spin isomers may stimulate also future reaction studies to explore their production and detection by fusion of two ions at high angular momenta [9,10]. For all these reasons, the investigation on toroidal high-spin isomers is of general interest.

In the liquid-drop model of a toroidal nucleus, we can select the major radius R, the minor radius d, the angular momentum $I = I_z$ about the symmetry axis, and the corresponding rigid-body moment of inertia $\Im_{\rm rigid}$ as macroscopic variables. (For a sketch of R and d, see Fig. 1 of [3].) The energy $I(I+1)/2\Im_{\rm rigid}$ associated with the angular momentum I can be called the "rotational" energy. The variation of the rotational energy and the Coulomb energy tend to counterbalance the variation of the surface energy [7]. As a consequence, there is an I-threshold above which the rotating toroidal nucleus can be stable against a variation of R/d. The toroidal nucleus is stable also against axially-asymmetric sausage distortions [3] within an I-window [7]. Beyond the I-window with $R/d \gg 1$, the sausage instabilities (known also as Plateau–Rayleigh instabilities, for review, see [11]) will break the toroid into sausages, which subsequently turn into beads (see e.g. Fig. 2 of [12]).

To study toroidal high-spin states theoretically, we need a systematic way to determine the quantized I value, which is a non-trivial function of N and Z. The quantized I can be obtained from the single-particle state diagrams under the constraint of a fixed aligned angular momentum. For simplicity, we limit our present studies to even–even $N = Z$ nuclei. Previously, an investigation of ^{40}Ca as the evolution of a chain of 10 alpha particles revealed that ^{40}Ca with $I = 60\hbar$ may represent a toroidal high-K isomeric state [13], in qualitative agreement with the I-threshold and I-window concepts in [7].

Accordingly, we need the energy diagram of the single-particle states in a toroidal nucleus for different aligned angular momenta I. For $I = 0\hbar$, the single-particle potential for a nucleon in a toroidal nucleus with azimuthal symmetry in cylindrical coordinates (r, z) can be represented by [3]

* Corresponding author.
E-mail addresses: stas@tytan.umcs.lublin.pl (A. Staszczak), wongc@ornl.gov (C.-Y. Wong).

http://dx.doi.org/10.1016/j.physletb.2014.10.013

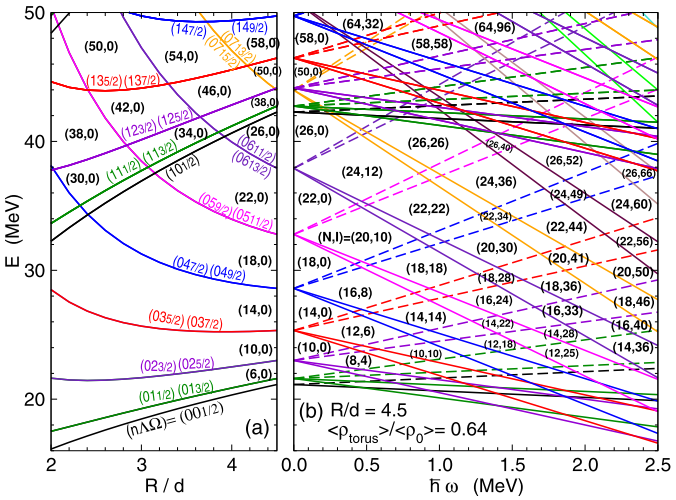

Fig. 1. (Color online.) (a) Single-particle states of a toroidal nucleus with $I = 0\hbar$ as a function of R/d, calculated with $\langle\rho_{\rm torus}\rangle/\langle\rho_0\rangle = 0.64$ and $A \sim 40$. Each state is labeled by (n, Λ, Ω), with $n = n_z + n_\rho$ and degenerate Ω_z. (b) Single-particle Routhians of a toroidal nucleus with $R/d = 4.5$, as a function of a cranking frequency $\hbar\omega$. Routhians of positive- and negative-Ω_z states are given by the solid and dashed lines, respectively. The listed pair numbers (N, I) refer to the occupation number N and the total angular momentum $I = I_z$ aligned along the symmetry z-axis.

$$V_0(r,z) = \frac{1}{2}m\omega_0^2(r-R)^2 + \frac{1}{2}m\omega_0^2 z^2, \tag{1}$$

where $\hbar\omega_0 = [(3\pi R/2d)^{1/3}41/A^{1/3}]\langle\rho_{\rm torus}\rangle/\langle\rho_0\rangle$. We have included the ratio $\langle\rho_{\rm torus}\rangle/\langle\rho_0\rangle$ where $\langle\rho_{\rm torus}\rangle$ and $\langle\rho_0\rangle$ are the average nuclear densities in the toroidal and the spherical configurations respectively, because the mean-field potential is proportional approximately to the nuclear density. In microscopic calculations, $\langle\rho_{\rm torus}\rangle/\langle\rho_0\rangle$ is found to be approximately 1/2 to 2/3. For $R \gg d$ and low-lying states with the radial nodal quantum number $n_\rho = 0$ and the azimuthal nodal quantum number $n_z = 0$, the expectation value of the spin–orbit interaction is approximately zero [3], and we can neglect the spin–orbit interaction.

We label a state by $(n\Lambda\Omega\Omega_z)$, where $n = (n_z + n_\rho)$, $\pm\Lambda$ is the z-component of the orbital angular momentum, and $\Omega = |\Lambda \pm 1/2|$ is the single-particle total angular momentum with z-components $\Omega_z = \pm\Omega$. For $R \gg d$, the single-particle energy of the $(n_\rho n_z \Lambda\Omega)$ state with $I = 0\hbar$ is therefore

$$E(n\Lambda\Omega) \sim \hbar\omega_0(n+1) + \frac{\hbar^2\Lambda^2}{2mR^2}. \tag{2}$$

Fig. 1(a) gives the single-particle state energies as a function of R/d for a toroidal nucleus with $I = 0\hbar$.

For a non-collectively rotating toroidal nucleus with aligned angular momentum, $I = I_z$, we use a Lagrange multiplier ω to describe the constraint $I_z = \langle\hat{J}_z\rangle = \sum_{i=1}^{N}\Omega_{zi}$. The constrained single-particle Hamiltonian becomes $\hat{h}' = \hat{h} - \omega\hat{J}_{zi}$, and the aligned angular momentum I is a step-wise function of the Lagrange multiplier ω [14], with each I spanning a small region of $\hbar\omega$. The single-particle Routhian with quantum numbers $(n\Lambda\Omega\Omega_z)$, under the constraint of the non-collective aligned angular momentum I is

$$E(n\Lambda\Omega\Omega_z) \sim \hbar\omega_0(n+1) + \frac{\hbar^2\Lambda^2}{2mR^2} - \hbar\omega\Omega_z. \tag{3}$$

Fig. 1(b) gives the single-particle Routhians as a function of the constraining Lagrange multiplier $\hbar\omega$, for a toroidal nucleus with $R/d = 4.5$, approximately the aspect ratio for many toroidal nuclei in this region. We can use Fig. 1(b) to determine $I = I_z$ as a function of N and $\hbar\omega$. Specifically, for a given N and $\hbar\omega$, the aligned I_z-component of the total angular momentum I from the N nucleons can be obtained by summing Ω_{zi} over all states below the Fermi energy.

There are shell gaps for different (N, I_z) configurations in Fig. 1. They represent configurations with relative stability for which additional shell corrections on top of the liquid-drop-type energy surface [15,3] may enhance the stability for toroidal configurations. The energy scales of the $\hbar\omega$ and E axes in Fig. 1(b) depend on N, R/d, $\langle\rho_{\rm torus}\rangle/\langle\rho_0\rangle$ which vary individually at different isomeric toroidal energy minima, but the structure of the (N, I_z) shells and their relative positions in Fig. 1(b) remain approximately the same in this $A \sim 40$ mass region. We can use Fig. 1(b) as a qualitative guide to explore the landscape of the energy surface for different (N, I_z) configurations, by employing a reliable microscopic model.

A microscopic theory that includes both the single-particle shell effects and the bulk properties of a nucleus is the Skyrme energy density functional approach in which we solve an equality-constrained problem:

$$\begin{cases} \min\limits_{\bar{\rho}} E^{\rm tot}[\bar{\rho}] \\ \text{subject to: } \langle\hat{N}_q\rangle = N_q, \\ \qquad\qquad \langle\hat{Q}_{\lambda\mu}\rangle = Q_{\lambda\mu}, \\ \qquad\qquad \langle\hat{J}_i\rangle = I_i, \end{cases} \tag{4}$$

where an objective function, $E^{\rm tot}[\bar{\rho}] = \langle\hat{H}_{Sk}\rangle$, is the Skyrme energy density functional [16]. The constraint functions are defined by average values of the proton/neutron particle-number operator, $\hat{N}_{p/n}$, the mass-multiple-moment operators, $\hat{Q}_{\lambda\mu}$, and the components of the angular momentum operator $\hat{J}_i$. $N_{p/n} = Z/N$ are the proton/neutron numbers, $Q_{\lambda\mu}$ are the constraint values of the multiple-moments, and I_i are the constraint components of the angular momentum vector.

The above constraint equations were solved using an augmented Lagrangian method [17] with the symmetry-unrestricted code HFODD [18]. In the particle-hole channel the Skyrme SkM* force [19] was applied and a density-dependent mixed pairing [20,21] interaction in the particle–particle channel was used. The code HFODD uses the basis expansion method in a three-dimensional Cartesian deformed harmonic oscillator basis. In the present study, we used the basis which consists of states having not more than $N_0 = 26$ quanta in the Cartesian directions, and not more than 1140 states.

Our objective is to locate local toroidal figures of equilibrium, if any, in the multi-dimensional search space of (A, Q_{20}, I). We first map out the energy landscape for axially-symmetric toroidal shapes under these Q_{20} and I constraints, with fine grids in Q_{20} and all allowed non-collective rotations in $0 \leqslant I \leqslant 132\hbar$ for different A. If the topographical landscape reveals a local energy minimum then the quadrupole constraint is removed at that minimum and free-convergence is tested to ensure that the non-collectively rotating toroid nucleus is indeed a figure of equilibrium.

For the case of $I = 0$, as shown in Fig. 2, the Skyrme–Hartree–Fock–Bogoliubov (HFB) calculations for $N = Z$ with $24 \leqslant A \leqslant 52$ reveal that as the quadrupole moment constraint, Q_{20}, decreases to become more negative, the density configurations with sphere-like geometry (open circles) turn into those of an axially-symmetric torus (full circles), as would be expected from the single-particle state diagrams of Fig. 1(a). The energies of axially-symmetric toroidal configurations as a function of Q_{20} lie on a slope. This indicates that even though the shell effects cause the density to become toroidal when there is a quadrupole constraint, the magnitudes of the shell corrections are not sufficient to stabilize the tori against the bulk tendency to return to sphere-like geometry.

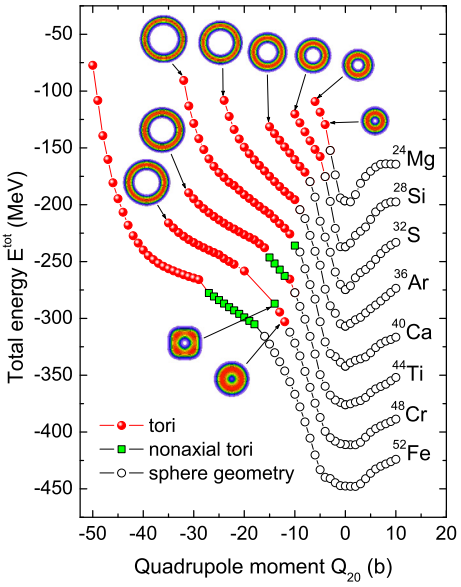

Fig. 2. (Color online.) The total HFB energy of ^{24}Mg, ^{28}Si, ^{32}S, ^{36}Ar, ^{40}Ca, ^{44}Ti, ^{48}Cr, and ^{52}Fe as a function of the quadrupole moment for the case of $I = 0$. Axially-symmetric toroidal configurations are indicated by the full circles, axially-asymmetric toroidal configurations by the full squares, and configurations with a sphere-like geometry by the open circles. Some toroidal density distributions are displayed.

We next extend our Skyrme–HFB calculations further to include both the quadrupole moment Q_{20} constraint and the angular momentum constraint, $I = I_z$. The pairing energies are smaller for toroidal nuclei than with a spherical geometry for a case of $I = 0$, additionally pairing interaction is suppressed as the two degenerate $\pm\Omega_z$ states split apart under the constraining $\hbar\omega$ when $I \neq 0$. We shall carry out the cranking calculations without the pairing interaction, using a Skyrme–HF approach. The results of such calculations for $28 \leqslant A \leqslant 48$ are presented in Fig. 3, where we plot the excitation energy of the high-spin toroidal states relative to the spherical ground state energy, $E^* = E^{\rm tot}(I) - E^{\rm tot}_{\rm g.s.}(0)$, as a function of the constrained Q_{20}, for different quantized I. For each point (Q_{20}, I) on an I curve for a fixed A, it was necessary to adjust $\hbar\omega$ judiciously within a range to ensure that the total aligned angular momentum of all nucleons in the occupied states gives the quantized I value of interest. The energy curves in Fig. 3 become flatter as I increases, similar to the energy curves in the liquid-drop model as the angular momentum increases [7].

With our systematic method outlined above, we are able to locate many high-spin toroidal isomeric states: ^{28}Si($I = 44\hbar$), ^{32}S($I = 48, 66\hbar$), ^{36}Ar($I = 56, 72, 92\hbar$), ^{40}Ca($I = 60, 82\hbar$), ^{44}Ti($I = 68, 88, 112\hbar$), ^{48}Cr($I = 72, 98, 120\hbar$), and ^{52}Fe($I = 52, 80, 104, 132\hbar$) as listed in Table 1. Note that with a fixed initial shape of a ring of 10 alpha particles, the earlier result of [13] finds only a single case of ^{40}Ca($I = 60\hbar$) as an isomeric toroidal figure of equilibrium. However, with the help of Fig. 1(b) and the fine grids in the large multi-dimensional space of (A, Q_{20}, I), we find a large number of isomers, demonstrating the general occurrence of toroidal high-spin states. The A and I values have their correspondences in the (N, I) shells in Fig. 1(b). The equilibrium configurations at the energy minima have been tested and found to be self-consistently free-converging after the removal of the quadrupole moment Q_{20} constraint.

Table 1 gives the properties of the high-spin toroidal isomers in $28 \leqslant A \leqslant 52$: their Q_{20}, $\hbar\omega$, and excitation energy E^* values, obtained with the Skyrme SkM* interaction. The excitation energy is of order 140–290 MeV. The toroidal density can be

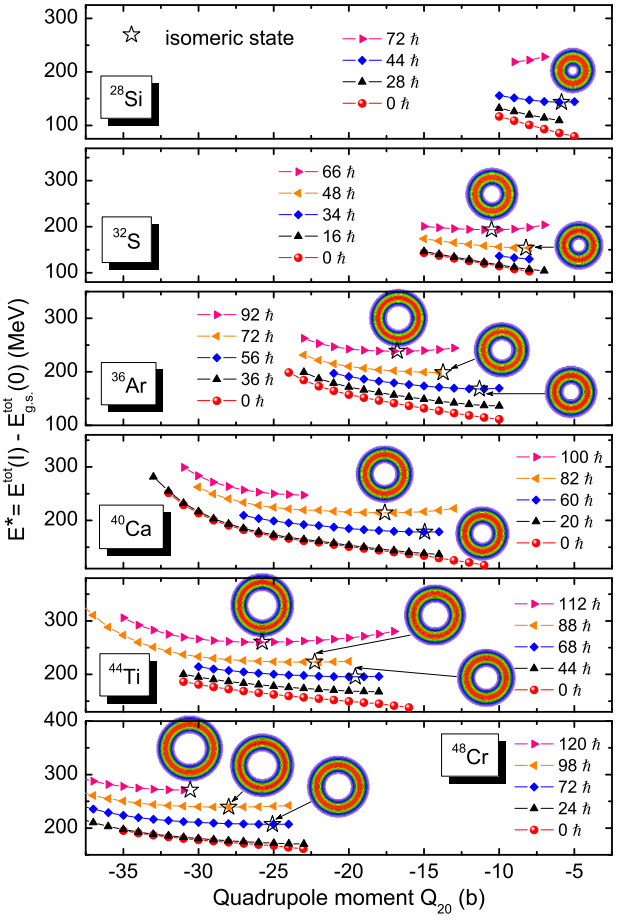

Fig. 3. (Color online.) The excitation energy of high-spin toroidal states (E^*) of ^{28}Si, ^{32}S, ^{36}Ar, ^{40}Ca, ^{44}Ti, and ^{48}Cr as a function of Q_{20} for different angular momentum along the symmetry axis, $I = I_z$. The density distributions and locations of isomeric toroidal energy minima are indicated by the star symbols.

Table 1
Properties of high-spin toroidal isomers at their local energy minima in $28 \leqslant A \leqslant 52$.

	$I/\hbar$	Q_{20} (b)	$\hbar\omega$ (MeV)	E^* (MeV)	R (fm)	d (fm)	R/d	$\rho_{\max}$ (fm^{-3})
^{28}Si	44	−5.86	2.8	143.18	4.33	1.45	2.99	0.119
^{32}S	48	−8.22	1.9	153.87	4.87	1.42	3.43	0.122
	66	−10.51	2.2	193.35	5.57	1.40	3.98	0.108
^{36}Ar	56	−11.31	1.7	168.03	5.44	1.40	3.88	0.125
	72	−13.73	1.85	198.63	6.04	1.39	4.34	0.113
	92	−16.78	2.0	238.56	6.73	1.37	4.91	0.103
^{40}Ca	60	−14.96	1.5	178.36	5.97	1.40	4.26	0.126
	82	−17.61	1.9	214.23	6.51	1.39	4.68	0.117
^{44}Ti	68	−19.57	1.2	195.46	6.55	1.39	4.71	0.128
	88	−22.27	1.4	223.09	7.01	1.38	5.08	0.120
	112	−25.76	1.6	260.24	7.56	1.37	5.52	0.113
^{48}Cr	72	−25.08	1.2	207.12	7.12	1.38	5.16	0.128
	98	−28.00	1.4	239.26	7.54	1.37	5.50	0.122
	120	−30.55	1.43	271.02	7.90	1.36	5.81	0.118
^{52}Fe	52	−29.24	0.8	202.86	7.39	1.38	5.35	0.134
	80	−31.43	0.95	227.54	7.68	1.38	5.56	0.130
	104	−33.54	1.3	252.65	7.94	1.37	5.79	0.126
	132	−35.62	1.5	288.91	8.20	1.36	6.03	0.123

parametrized as a Gaussian function, $\rho(r, z) = \rho_{\max} \exp\{-[(r - R)^2 + z^2]/(d^2/\ln 2)\}$, where R, d, and $\rho_{\max}$ for isomeric states are listed. While the major radius R and R/d increase with increasing A, the minor radius d remains to be approximately the same.

We plot in Fig. 4 the density distributions of the toroidal configurations of ^{40}Ca with $I = 60\hbar$ as a cut in the radial x-direction for

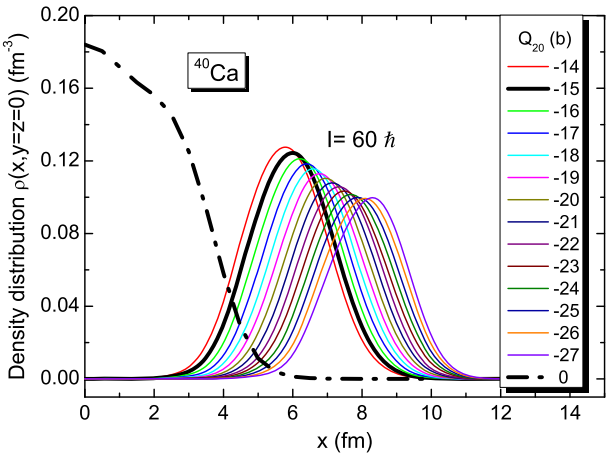

Fig. 4. (Color online.) The density distributions of ^{40}Ca for $I = 60\hbar$ as a cut in the radial direction x for different Q_{20}: (i) the thick solid curve is for the equilibrium toroidal configurations at the local energy minimum at $Q_{20} = -15$ b, (ii) the thin line curves are for the other Q_{20} as labeled, and (iii) the dash–dot curve is for ^{40}Ca in the spherical ground state.

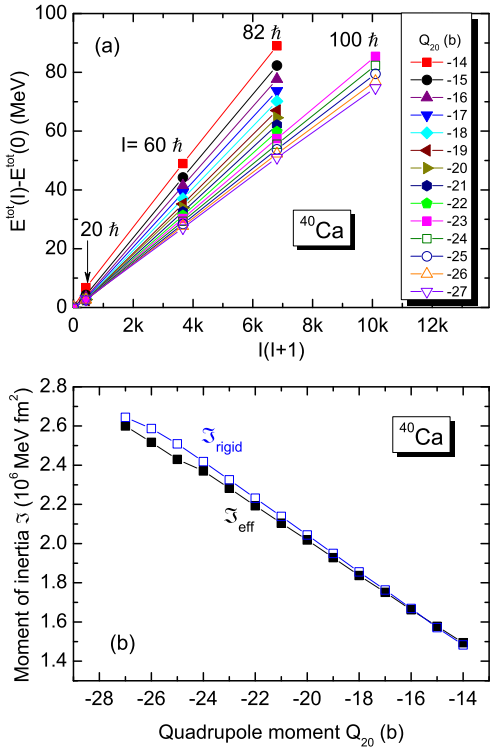

Fig. 5. (Color online.) (a) The total energy difference $E^{\rm tot}(I) - E^{\rm tot}(0)$ as a function of $I(I+1)$ for toroidal ^{40}Ca at different Q_{20}. The inverses of the slopes of different lines give the effective moments of inertia $\Im_{\rm eff}$. (b) The effective moments of inertia $\Im_{\rm eff}$ and the rigid body moments of inertia $\Im_{\rm rigid}$ as a function of Q_{20} for toroidal ^{40}Ca.

different Q_{20}. One notes that the average density for ^{40}Ca($I = 60\hbar$) at the toroidal energy minimum of $Q_{20} = -15$ b (thick solid curve) is only 0.64 of the average nuclear density for a spherical ^{40}Ca (dash–dot curve).

To gain new insights into the nature of the non-collective rotational motion, we determine an effective moment of inertia $\Im_{\rm eff}$ for toroidal ^{40}Ca from the total energy of the system as a function of I as $E^{\rm tot}(I) = E^{\rm tot}(0) + I(I+1)/2\Im_{\rm eff}$. Using the results in Fig. 3, we find in Fig. 5(a) that such a linear dependence between $E^{\rm tot}(I) - E^{\rm tot}(0)$ and $I(I+1)$ holds for different Q_{20}. An effective moment of inertia $\Im_{\rm eff}$ can be extracted as a function of Q_{20}. On the other hand, for different Q_{20}, one can calculate the rigid-body moment of inertia $\Im_{\rm rigid} = m_N 2\pi^2 R(d^2/\ln 2)\rho_{\max}[R^2 + 3/(2\ln 2)d^2]$ from the density distributions in Fig. 4. The comparison of $\Im_{\rm eff}$ and $\Im_{\rm rigid}$ in Fig. 5(b) indicates the approximate equality of $\Im_{\rm eff}$ and $\Im_{\rm rigid}$. This is in agreement with the result of Bohr and Mottelson who showed that the moment of inertia associated with the alignment of single-particle orbits along an axis of symmetry is equal to the rigid-body moment of inertia [22] and justifies the use of $\Im_{\rm rigid}$ in the earlier liquid-drop model of a rotating toroidal nucleus in [7].

It is clear from Fig. 1(b) that large shell effects are expected for some odd N and Z at various I values, and for combining different (N, I_N) with (Z, I_Z) at the same $\hbar\omega$. Hence light toroidal nuclei with odd-N, odd-Z, and $N \neq Z$ may be possible. The large shell gaps for $(N, I) = (58, 58\hbar)$, $(64, 32\hbar)$, and $(64, 96\hbar)$ call for future exploration of high-spin toroidal isomers in the mass region of $A \sim 120$.

In conclusion, under the considerations of the aligned single-particle angular momentum and the bulk behavior, the constrained self-consistent Skyrme–Hartree–Fock model calculations reveal that high-spin toroidal isomers may have general occurrences in the mass region of $28 \leqslant A \leqslant 52$. Experimental search for these nuclei may allow the extraction of the bulk properties of this new type of nuclear fluid and its possible utilization as a source of energy.

Acknowledgements

The authors wish to thank Drs. Jerzy Dudek, Vince Cianciolo, and I-Yang Lee for helpful discussions. This work was supported in part by the Division of Nuclear Physics, U.S. Department of Energy, U.S.A., Contract No. DE-AC05-00OR22725.

References

[1] See a reference to J.A. Wheeler's toroidal nucleus in G. Gamow, Biography of Physics, Harper & Brothers Publishers, New York, 1961, 297 pp.
[2] C.Y. Wong, Phys. Lett. B 41 (1972) 446–450.
[3] C.Y. Wong, Ann. Phys. (N.Y.) 77 (1973) 279–353.
[4] G. Royer, F. Haddad, B. Jouault, Nucl. Phys. A 605 (1996) 403–416.
[5] V. Zherebchevsky, et al., Phys. Lett. B 646 (2007) 12–18.
[6] A. Staszczak, C.Y. Wong, Acta Phys. Pol. B 40 (2008) 753–757, and references cited therein.
[7] C.Y. Wong, Phys. Rev. C 17 (1978) 331–340.
[8] A. Bohr, B.R. Mottelson, Nucl. Phys. A 354 (1981) 303c–316c.
[9] Ph. Eudes, Z. Basrak, F. Sébille, V. de la Mota, G. Royer, M. Zoric, J. Phys. Conf. Ser. 420 (2013) 012133-1–012133-8.
[10] H. Esbensen, Phys. Rev. C 85 (2012) 064611-1–064611-9.
[11] J. Eggers, Rev. Mod. Phys. 69 (1997) 865.
[12] E. Pairam, A. Fernández-Nieves, Phys. Rev. Lett. 102 (2009) 234501.
[13] T. Ichikawa, J.A. Maruhn, N. Itagaki, K. Matsuyanagi, P.-G. Reinhard, S. Ohkubo, Phys. Rev. Lett. 109 (2012) 232503-1–232503-4.
[14] P. Ring, P. Schuck, The Nuclear Many-Body Problem, Springer-Verlag, Berlin, Heidelberg, New York, 1980, 142 pp.
[15] M. Brack, J. Damgaard, A.S. Jensen, H.C. Pauli, V.M. Strutinsky, C.Y. Wong, Rev. Mod. Phys. 44 (1972) 320–405.
[16] D. Vautherin, D.M. Brink, Phys. Rev. C 5 (1972) 626;
Y.M. Engel, D.M. Brink, K. Goeke, S. Krieger, D. Vautherin, Nucl. Phys. A 249 (1975) 215.
[17] A. Staszczak, M. Stoitsov, A. Baran, W. Nazarewicz, Eur. Phys. J. A 46 (2010) 85–90.
[18] N. Schunck, et al., Comput. Phys. Commun. 183 (2012) 166–192.
[19] J. Bartel, P. Quentin, M. Brack, C. Guet, H.B. Håkansson, Nucl. Phys. A 386 (1982) 79–100.
[20] J. Dobaczewski, W. Nazarewicz, M.V. Stoitsov, Eur. Phys. J. A 15 (2002) 21–26.
[21] A. Staszczak, A. Baran, J. Dobaczewski, W. Nazarewicz, Phys. Rev. C 80 (2009) 014309-1–014309-6.
[22] A. Bohr, B.R. Mottelson, Nuclear Structure. Vol. II: Nuclear Deformations, World Scientific, Singapore, New Jersey, Hong Kong, 1998, p. 80.